Ultrasound in Medicine & Biology 000 (2023) 1−7

Contents lists available at ScienceDirect

Ultrasound in Medicine & Biology

journal homepage: www.elsevier.com/locate/ultrasmedbio

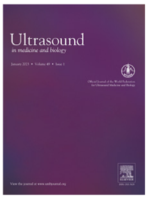

Original Contribution

High-Frame-Rate Volumetric Porcine Renal Vasculature Imaging

Luxi Wei [a,*], Geraldi Wahyulaksana [a], Maaike te Lintel Hekkert [a], Robert Beurskens [a], Enrico Boni [b], Alessandro Ramalli [b], Emile Noothout [c], Dirk J. Duncker [a], Piero Tortoli [b], Antonius F.W. van der Steen [a,c], Nico de Jong [a,c], Martin Verweij [a,c], Hendrik J. Vos [a,c]

[a] *Department of Cardiology, Erasmus MC University Medical Center, Rotterdam, The Netherlands*
[b] *Department of Information Engineering, University of Florence, Florence, Italy*
[c] *Department of Imaging Physics, Delft University of Technology, Delft, The Netherlands*

ARTICLE INFO

Keywords:
Contrast-enhanced
High frame rate
In vivo
Vasculature
Volumetric
3-D ultrasound
Kidney

Objective: The aim of this study was to assess the feasibility and imaging options of contrast-enhanced volumetric ultrasound kidney vasculature imaging in a porcine model using a prototype sparse spiral array.

Methods: Transcutaneous freehand *in vivo* imaging of two healthy porcine kidneys was performed according to three protocols with different microbubble concentrations and transmission sequences. Combining high-frame-rate transmission sequences with our previously described spatial coherence beamformer, we determined the ability to produce detailed volumetric images of the vasculature. We also determined power, color and spectral Doppler, as well as super-resolved microvasculature in a volume. The results were compared against a clinical 2-D ultrasound machine.

Results: Three-dimensional visualization of the kidney vasculature structure and blood flow was possible with our method. Good structural agreement was found between the visualized vasculature structure and the 2-D reference. Microvasculature patterns in the kidney cortex were visible with super-resolution processing. Blood flow velocity estimations were within a physiological range and pattern, also in agreement with the 2-D reference results.

Conclusion: Volumetric imaging of the kidney vasculature was possible using a prototype sparse spiral array. Reliable structural and temporal information could be extracted from these imaging results.

Introduction

The diagnosis and monitoring of acute kidney diseases, chronic kidney diseases and kidney transplants can be significantly boosted by the assessment of blood flow and vasculature structure on the local and global scales [1,2]. For instance, the identification of local ischemic or hypoperfused regions can be used to diagnose vessel stenosis, perfusion deficit and allograft rejection [3−6]. Organ perfusion is also an important quality index of organ health, and can be evaluated indirectly through the resistive index (RI). RI is derived from spectral Doppler measurements and is an indicator of microcirculation impedance [3,7]. Perfusion also needs to be assessed on a regional level in cases of post-interventional monitoring and treatment guidance in acute kidney injuries, especially after interventions [3,8]. For these reasons, it is important to have a reliable method of imaging renal vasculature and blood flow on both the capillary and arterial/venous levels.

Renal perfusion and blood flow are currently measured using a few imaging modalities. Computed tomography and magnetic resonance imaging can image true perfusion and blood flow in three dimensions but require the use of ionizing radiation or nephrotoxic contrast agents [3,9,10]. Conventional 2-D ultrasound can assess blood flow and structure of the kidney, and is often the first imaging technique to be performed when kidney diseases are suspected [3,11]. With the addition of contrast agents and state-of-the-art processing, ultrasound can be used to visualize small vessels, even smaller than the diffraction limit [12,13]. Such a super-resolution imaging technique provides additional information on vessel tortuosity or flow rates on the capillary level, which can be indicators of perfusion quality [14,15]. However, conventional 2-D ultrasound is limited to the investigation of a single slice of the organ at a time. This can potentially lead to misdiagnosis when the region of interest is not intercepted or out-of-plane motion causes visual vessel misalignments, yielding to “ghost vessels.” Volumetric ultrasound is a solution to these drawbacks. Motion correction can be obtained by eliminating effects from lateral tissue and probe motion, improving reconstructions of small vessels and reducing ghost vessel artifacts. In addition, flow directions and flow rates can be estimated in the volume, reconstructing more complete flow dynamics information and removing errors caused by out-of-plane flow. These benefits can lead to improved diagnostics, disease monitoring and intervention guidance [5,16,17].

A method of achieving volumetric contrast-enhanced ultrasound imaging is by use of 2-D sparse arrays [18]. Sparse arrays enable high-frame-rate (>1000 frames/s [FPS]) volumetric imaging with relatively

---

[*] Corresponding author. Department of Cardiology, Erasmus MC University Medical Center, Doctor Molewaterplein 40, CA Rotterdam 3000, The Netherlands.
E-mail address: l.wei@erasmusmc.nl (L. Wei).

https://doi.org/10.1016/j.ultrasmedbio.2023.08.009
Received 30 March 2023; Revised 2 July 2023; Accepted 8 August 2023

0301-5629/© 2023 The Author(s). Published by Elsevier Inc. on behalf of World Federation for Ultrasound in Medicine & Biology. This is an open access article under the CC BY license (http://creativecommons.org/licenses/by/4.0/)

Please cite this article as: L. Wei et al., High-Frame-Rate Volumetric Porcine Renal Vasculature Imaging, Ultrasound in Medicine & Biology (2023), https://doi.org/10.1016/j.ultrasmedbio.2023.08.009

low hardware requirements. The high frame rates are beneficial for fast flows in large vessels and enable frame-by-frame tracking of single bubbles in the capillaries. Sparse arrays are especially suited for microbubble imaging because of their inherently low transmit/receive efficiency: low transmit pressures avoid bubble disruption, while the scattered signal is high because of bubble resonance and has lower requirements on the receive sensitivity. Previously, Harput et al. [19] illustrated 3-D super-resolution using sparse apertures in an *in vitro* setup, and Wang et al. [20] obtained preliminary volumetric contrast-enhanced images in a rabbit kidney using sparse apertures, but without detailing the methods or discussing the results. A spiral implementation of sparse arrays has been found to perform focused-beam or multiline imaging [21,22]. Single beams can also be used for more accurate spectral Doppler measurements, enabling volumetric flow estimation [23]. However, these methods have either limited frame rates or limited field-of-view for our goal.

For vascular imaging using microbubbles, our group has previously designed, manufactured and characterized sparse arrays in a spiral layout [24]. An earlier probe prototype was used for imaging a tissue-mimicking phantom and chicken embryos [25]. The phantom provided uniform tissue-like scattering, while the chicken embryo provided physiological blood flow in a low-scattering structure. A spatial coherence-based beamformer (SC beamformer) was also developed in [25] to reduce clutter and increase contrast. In this new study, such a SC beamformer is used to determine the feasibility of transcutaneous volumetric imaging of healthy porcine kidneys. Tissue scattering, attenuation and motion make porcine kidneys more challenging than the previous models. We illustrate a range of imaging options with this probe by showing 3-D SC beamformed volumes, power, color and spectral Doppler, as well as super-resolved microvasculature results.

Methods

Animal and microbubble preparations

Two female Yorkshire × Norwegian Landrace pigs (35 and 36 kg, respectively) were sedated with intramuscular injections of Zoletil 50 (6 mg/kg), xylazine (2.25 mg/kg) and atropine (0.03 mg/kg), anesthetized with intravenous infusion of pentobarbital (10−15 mg/kg/h), intubated and mechanically ventilated. The animal experiments followed European Union and institutional guidelines for the care and use of laboratory animals, with local Centrale Commissie Dierproeven approval AVD1010020172411 (SP2100125). A diluted (30 × in saline) Definity solution (Lantheus Medical Imaging Inc., North Billerica, MA, USA) was infused through the jugular vein at 6 and 1 mL/min flow rates.

Imaging methods

Volumetric imaging was performed using a homemade sparse array centered at 5 MHz with a bandwidth of 32%. More information on the transducer characteristics can be found in [24]. The probe used in the work described here was finally enclosed in a probe holder (Fig. 1), thus enabling the complex animal studies described here. This probe was driven by a Vantage 256 system (Verasonics Inc., Kirkland, WA, USA). A homemade system was developed to record the electrocardiogram (ECG) signal, detect the R-peak and trigger the volumetric recordings. The system comprised an ECG machine (CT-1000 cardiotachometer, CWE Inc., Ardmore, PA, USA), an oscilloscope (TDS3014B, Tektronix, Beaverton, OR, USA) and a USB oscilloscope with recording software (Handyscope, TiePie Engineering, Sneek, Netherlands). The ECG triggering and recording system allowed comparison between the volumetric and clinical system spectral recordings.

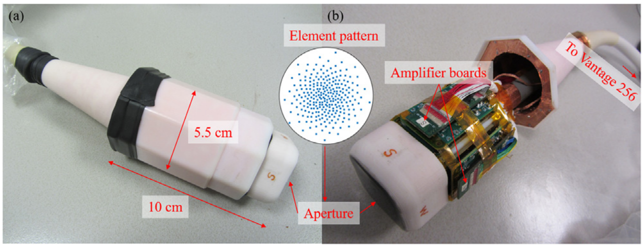

Figure 1. (a) Fully assembled spiral array. (b) Inside the 3-D-printed holder there are four printed circuit boards with 256 amplifiers in total, amplifying receive signal from each element [26]. Micro-coaxial wires run inside a flexible cable to the Vantage 256 system.

Volumetric imaging of the left kidney was performed by freehand scanning the pig lying on its right side, and under free-breathing (protocol 1) or breath-hold (protocols 2 and 3) conditions. Three-cycle positive polarity transmit pulses were used for all acquisitions, with peak positive pressures of around 40 kPa at 3 cm depth for the diverging transmits (measured via hydrophone; plane wave transmit fields were not measured). As summarized in Table 1, a scan sequence based on the transmission of either five steered diverging waves (protocols 1 and 2: 30° opening angle, 5° steering angle) or one steered (protocol 3: 5° steering angle) plane wave were used. For protocol 1, the center 120 elements were used for transmission to increase the uniformity of the transmit field [25]. Further information on the diverging wave transmission sequence can be found in an earlier report [25]. For protocol 3, a steering angle was applied to the plane wave transmission to reduce load on the system. A 5 kHz pulse repetition frequency enabled 5 and 1 kHz frame rates for the one- and five-angled sequences, respectively. Two-second-long acquisitions were performed, long enough to capture more than two cardiac cycles. The collected radiofrequency (RF) data were sampled four times per period of the central frequency (20 MHz) and stored for further post-processing.

To confirm the vasculature pattern that we observed in three dimensions, for pig 2, conventional 2-D B-mode, contrast-enhanced and spectral Doppler images were also acquired with a clinical machine (Zonare ZS3, P7-3C and P4-1C probes, Mindray Innovation Center, San Jose, CA, USA). For the comparison of clinical contrast-enhanced images and the 3-D results, the 2-D imaging probes were placed roughly across the y-axis center of the 3-D probe to capture images in the xz plane. However, angular rotation and tissue deformation could not be avoided to achieve a complete match between the experimental volumetric data sets and these 2-D reference frames. For spectral Doppler acquisitions, arteries were first identified using color Doppler. Then the range gate was placed at the location of a large, pulsating artery. The spectrum of this artery was then recorded.

Beamforming methods

Two beamforming methods were used in the work described here and will be referred to in the subsequent post-processing section. The conventional delay-and-sum (DAS) beamforming was performed using the Ultrasound Toolbox [27]. The SC beamformer, as described in our previous publication [25], uses the coherency of received signal between different elements to suppress spatially incoherent clutter signal and retain coherent microbubble signal. Similar to DAS beamforming, for each sub-volumetric acquisition, dynamic receive focusing was applied to the in-phase/quadrature demodulated channel-domain data obtaining a "delayed matrix." For each voxel of interest, the average signal coherence (sc_{voxel}) between all non-repeating channel pairs (i, j) was computed by

$$sc_{\mathrm{voxel}} = \frac{\sum_{j<i,i=1}^{N} s(i)s^{*}(j)}{\sqrt{\sum_{j<i,i=1}^{N}\left|s(i)\right|^{2}\cdot\sum_{j<i,i=1}^{N}\left|s(j)\right|^{2}}} \tag{1}$$

where $s(i)$ is the signal received by element i from the specific voxel of interest, and $s^{*}(j)$ is the complex conjugate of the signal received by element j. The non-zero real part of the correlation values was log

Table 1
Experimental parameters

Protocol	No. of elements (Tx/Rcv)	Opening angle (°)	Steering angles (°)	PRF (Hz)	Frame rate (Hz)	Infusion rate (mL/min)	Breath-hold	Pig No.
1	120/256	30 (diverging waves)	(0,0); (0,5); (5,0); (0,−5); (−5,0)	5000	1000	6	No	1
2	120/256	30 (diverging waves)	(0,0); (0,5); (5,0); (0,−5); (−5,0)	5000	1000	1	Yes	2
3	256/256	0 (plane waves)	(0,5)	5000	5000	1	Yes	2

PRF, pulse repetition frequency; Rcv, receive; Tx, transmit.

compressed for display. As the SC beamformer also uses the "delayed matrix," an intermediate step of the DAS beamformer, the two were calculated simultaneously for every volume to reduce computational time. As a reference, beamforming one volume in two ways (DAS and SC) took around 0.6 s with a 24-core CPU computer with no restraint on RAM.

Post-processing methods

To visualize the vasculature, radiofrequency (RF) echo data were acquired at high contrast injection rates (6 mL/min) and suitably processed. First, a singular-value-decomposition (SVD) filter was used at an ensemble length of 50 frames. The first three to four ranks were empirically chosen and removed to visually reject the tissue signal. The filtered RF data were then SC beamformed [25] to suppress grating lobes and side lobes, producing images at higher contrast. For comparison purposes, the same filtered data were also beamformed with the DAS method. Power Doppler images were then produced using the lag 0 autocorrelation function with 10-frame ensembles. Rigid translational motion was estimated in three dimensions using the power Doppler data [28], and this motion was compensated for in both power Doppler and SC beamformed volumes to remove breathing artifacts.

To better visualize the microvasculature, super-resolution processing was performed on renal cortex vessels using a 3-D-adapted version of the algorithm described in [29]. The steps include the segmentation of individual bubbles by masking based on voxel intensity, followed by the estimation of their centers of mass. To further differentiate the bubble signal from noise, the Hungarian algorithm was used to track bubble motion through time.

To avoid aliasing in larger vessels, color Doppler and spectral Doppler were calculated from the one-angle plane wave 5 kHz scan sequence. Color Doppler results were calculated using the lag-1 correlation function with 10-frame ensemble length, leading to a 500 Hz volume rate. The color Doppler results were also motion corrected using the shifts estimated from the power Doppler. An artery was selected for 3-D spectral Doppler processing. This artery was at approximately the same location on the clinical system spectral Doppler recordings. The artery was manually segmented by drawing a cylinder in three dimensions along the length of the artery. Spectral Doppler was calculated using an ensemble length of 50 frames, with 10 frames of overlap, over the 2 s of acquisition. The Doppler angle was also estimated based on the segmentation and used to convert Doppler frequencies to speed. Peak-systolic and end-diastolic speeds were estimated by visual inspection for every visible cardiac cycle.

Results

Figure 2 is a render of the time-averaged SC-beamformed volumetric vasculature obtained from a sample protocol 1 acquisition. The high microbubble infusion rate enabled the visualization of small vessels in the renal cortex after 3-D motion correction. Interlobular vessels were also visualized, and the 3-D tree-shaped structure could be identified. Maximum intensity projections onto three orthogonal planes are also visualized in Figure 2. Note that the projected vessels look denser than in conventional 2-D acquisitions because of the differences in effective slice thicknesses.

Figure 3 illustrates sample slices through the same volume. On individual slices, the renal medulla produces gaps between the interlobular vessels. Because of the low blood volume and low flow in the vasculature, the microbubble signal in these regions was likely removed by the SVD filter. Three-dimensionally rendered videos of time-averaged volumes can be found in the supplementary material (Videos S1 and S2, online only).

Figure 4 allows comparison of B-mode and contrast-enhanced images taken using a clinical ultrasound machine and a contrast-enhanced image obtained with the sparse array. Almost the entire kidney was captured using B-mode ultrasound (Fig. 4a). The oval shape of the kidney cross-section, as well as the renal pelvis, can be seen. In contrast mode, the microbubbles and hence the vasculature could be seen (Fig. 4b). Looking at the region highlighted in *red*, a similar contrast-enhanced 2-D slice was found in the volumetric recording with the sparse array (Fig. 4c). The shape of the renal pelvis and adjacent low-blood-flow regions of a selected 2-D slice roughly matches that in the clinical image (Fig. 4b, 4c). Although the vasculature patterns are very similar, they do not match exactly because of deformations during imaging and slightly different imaging angles. More complete vasculature in the renal cortex can be seen in the high-frame-rate 2-D slice because more frames were recorded and accumulated. As an estimate of the image quality of the high-frame-rate recordings compared with that of a 2-D clinical machine, we estimated the lateral and axial point-spread-function (PSF) size and background level of the images in Figure 4. For a slice of our high-frame-rate volumetric recording, the estimated lateral and axial PSF sizes for a scatterer located at a 24 mm depth (Fig. 4b, *turquoise arrowhead*) are 1.3 and 0.7 mm respectively. Similar slices obtained from the clinical system for a scatterer located at a 20 mm depth (Fig. 4a, *turquoise arrowhead*) are 0.6 and 0.4 mm for lateral and axial PSF, respectively. Contrast-wise, the high-frame-rate slice result has a background value of −20 dB (calculated using the *turquoise boxed region* in Fig. 4b), whereas the clinical machine result has a background value

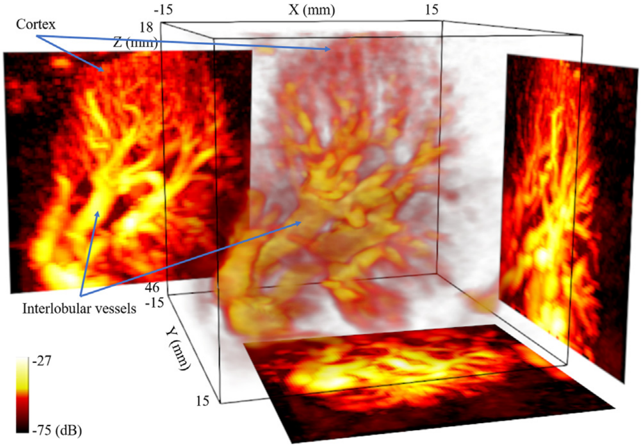

Figure 2. Three-dimensional render of a sample acquisition after *spatial coherence-based* beamforming and temporal averaging. The maximum intensity projections onto the three orthogonal planes are displayed next to the render. A 3-D rendered video of this data set can be found in the supplementary material (online only).

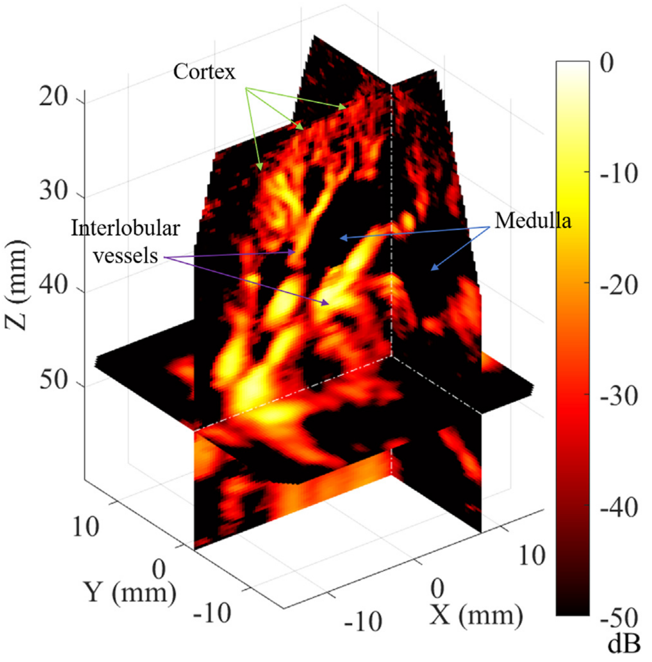

Figure 3. Slices of the time-averaged beamformed volume in three orthogonal planes. The planes were selected to resemble conventional 2-D images, where the interlobular vessels (***purple arrows***) and capillaries in the cortex (***green arrows***) can be seen. The renal medulla (***blue arrows***) can also be identified as the low-blood-flow region between the interlobular vessels.

of −34 dB (calculated using the *turquoise boxed region* in Fig. 4a). These results give a rough estimate of the image quality of the high-frame-rate recordings.

In the kidney cortex, there are mainly small vessels (<15 µm) [30] that contain slow blood flow. In this region (between 1.8 and 2.8 cm in depth) of Figure 4c, single microbubbles could be distinguished flowing through the microvasculature. Figure 5a is the maximum-intensity projection against the y-plane of frame 1 of a power Doppler time series, where individual bubbles could be seen in the cortex. As more frames were accumulated (Fig. 5b, 5c), a more complete vasculature structure appeared. However, because of the low resolution, the vessel structure can be seen only after 3-D super-resolution processing (Fig. 5d) of 2-s-long freehand recordings. This confirms the possibility of microvasculature imaging in three dimensions. Microbubble flow direction was measured using the localized tracks (Fig. 5e). Vessels with bubbles flowing upward (*red*) or downward (*blue*) were identified. They were oriented roughly parallel to each other, in agreement with kidney cortex vessel structure from histology.

Lastly, we also demonstrate the possibility of contrast-enhanced volumetric Doppler. The acquisitions at 5 kHz frame rates (protocol 3) were used to estimate blood flow speeds of the interlobular arteries and veins. Figure 6c is an overlay of one slice in the color Doppler volumetric image on the same focused beam B-mode slice. The *green circle* indicates the vessel of interest on this plane. This artery was manually segmented in three dimensions, and the segmentation mask is shown in Figure 6d in *green*, where it can be seen crossing the different planes. The average spectrum of the segmented artery is provided in Figure 6e, with its simultaneously acquired ECG trace in *yellow*. The pulsation of this artery could be observed, with high flow following the R-peak of the ECG signal. When we looked at the same vessel using the clinical system (Fig. 6a), we found similar pulsations within the same speed range (Fig. 6b, 6e). We found the peak-systolic speed and end-diastolic speed measured from the clinical system to be 0.41 ± 0.02 m/s and 0.19 ± 0.02 m/s, respectively. For the volumetric recording, we found the peak-systolic speed and end-diastolic speed to be 0.43 ± 0.01 m/s and 0.21 ± 0.00 m/s, respectively.

Discussion

In this article, we have described our *in vivo* porcine renal vasculature volumetric imaging results. Using our home-built sparse spiral array, we developed various imaging strategies for the current imaging modalities.

Figures 2 to 4c illustrate that by transmitting diverging waves combined with angular compounding and spatial coherence beamforming, the cortex microvasculature as well as the larger interlobular vessels can be imaged. We could match a slice of our volume to a similar plane imaged using a clinical machine, thus visually confirming the anatomy. Even though we tried to line up the clinical probe and our sparse spiral array such that they imaged the same plane during the experiment, it was difficult to control the position and especially the angle because of the stretching or pressing of the tissue. Also for this reason, the depth range of the structures of interests are not exactly the same in Figure 4.

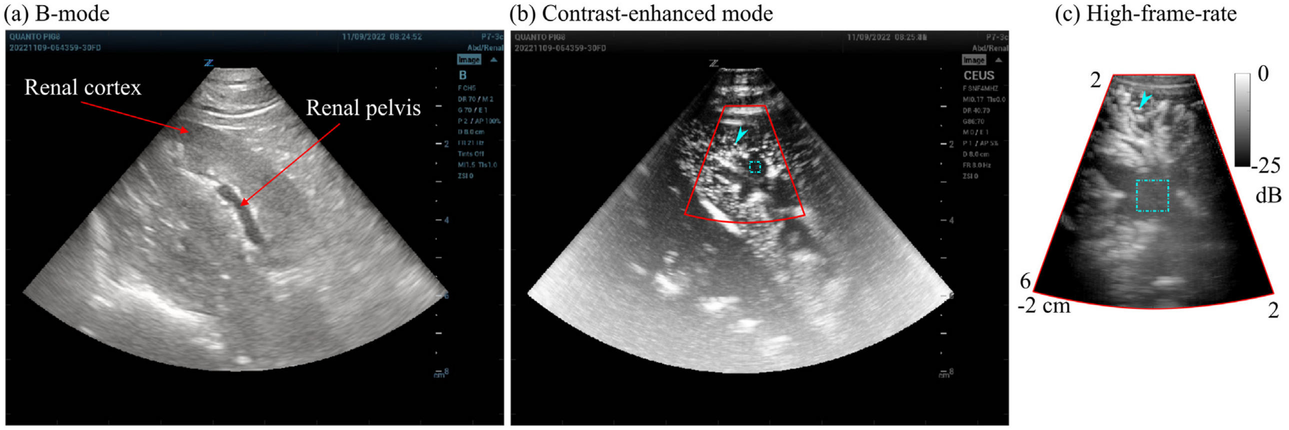

Figure 4. Comparison between 2-D images from a clinical system (a, b) using a P7-3C probe (Zonare, San Jose, CA, USA) and a slice of the volumetric image (c). (a) B-mode image of the kidney captured using the clinical system. The kidney can be seen from around a 1.5 cm depth down to around a 5.5 cm depth. The renal cortex is visible as a hypo-echoic elliptical region in the center of the kidney. (b) In contrast-enhanced mode of the clinical system, microbubbles in the vasculature are visible while tissue signal was suppressed. The ***red box*** approximately outlines the region that corresponds to the slice from the volumetric high-frame-rate capture (c). (c) One slice of power Doppler-processed volume of the same kidney. The hypo-echoic region in the center resembles the outlined region in (b). In both (a) and (b), the ***turquoise arrowheads*** and the ***boxed regions*** were used to estimate for point spread function and background level. The differences in depth between the clinical and high-frame-rate systems was likely caused by pressing of the probe and imaging angle differences.

Yet, because of the visual similarities of these slices, we think there is a good qualitative match between our volumetric and the clinical results.

Thanks to our high frame rate (1 kHz), we could track single microbubbles in the kidney cortex and form 3-D super-resolved vasculature images (Fig. 5). For these microbubbles, the direction and presence of blood flow could be calculated in these small vessels, yielding more direct perfusion information. Interestingly, we could not distinguish glomeruli in our recordings. We think that because of the slow flow speed and the presence of tissue motion, the SVD filter removed signal coming from the glomeruli and other vessels with extremely slow flow. Better filtering strategies, or contrast-specific imaging, should be investigated.

Lastly, we determined that when frame rates are further increased (to 5 kHz) by transmitting unsteered plane waves, high flow rates within larger vessels can be measured (Fig. 6). The high frame rate-enabled axial speed estimation of up to 0.4 m/s, sufficient to measure blood flow in the interlobular vessels (max 0.45 m/s in three dimensions as measured by spectral Doppler [Fig. 6e]). Spectral Doppler was performed using the volumetric data, and the results roughly match those obtained using a clinical machine (around 0.02 m/s higher). As our measurements were performed in three dimensions, problems in conventional flow estimations (such as out-of-plane flow) were avoided and proper angle correction could be performed, yielding theoretically more accurate results. The accuracy of the velocity estimations can theoretically be further improved. Automated vessel segmentation can be incorporated to calculate the vessel angle anywhere in space, and spectral Doppler with focused beams can be used to reduce influences from side lobes of adjacent scatterers. But more importantly, the amount of improvement in diagnostic value that volumetric spectral Doppler brings needs be assessed first.

The volumetric imaging ability might be used for other organs as well. Vasculature structures at shallow depths would all be suitable to image using this 5 MHz center frequency array. For instance, determining the tumor perfusion can help with an early diagnosis, and the 3-D view can reduce false negatives caused by incorrect probe positioning and, therefore, an incorrect 2-D projection/view [17]. Furthermore, the 3-D tracking of bubbles close to carotid plaques may yield information on shear stresses in the fluid and hence in the plaques [31]. in addition to 3-D vascular structure imaging of the brain (post-craniotomy), blood flow dynamics related to metabolism and neural activation could potentially be measured thanks to the high frame rates [32].

With the advantage of reduced channel counts and ease of use, the sparse arrays come with the drawbacks of having low transmit power, lower receive sensitivity and high clutter levels. However, microbubbles are perfect imaging targets for sparse arrays, where low transmission pressures are required to prevent bursting, and their scattered signal is high. We further increased the reception sensitivity of the probe by incorporating receive pre-amplifiers, providing 27 dB signal-to-noise ratio improvement over direct element connections [26]. Tissue suppression was enabled by SVD processing, and high clutter levels were suppressed by using coherence-based SC beamforming [25]. As an estimate of image quality, the lateral and axial PSF sizes and background level on the clinical contrast-enhanced image and a slice of the high-frame-rate image were calculated and compared (Fig. 4). The resolution and background levels were not as good as the clinical system results, but this is to be expected when considering the aperture sizes and number of transducer elements. Volumetric probes of similar operating frequencies and high frame rates such as the transesophageal echocardiography matrix array and the row-column array have reported similar resolutions [33,34] and worse contrast [34]. All in all, by using

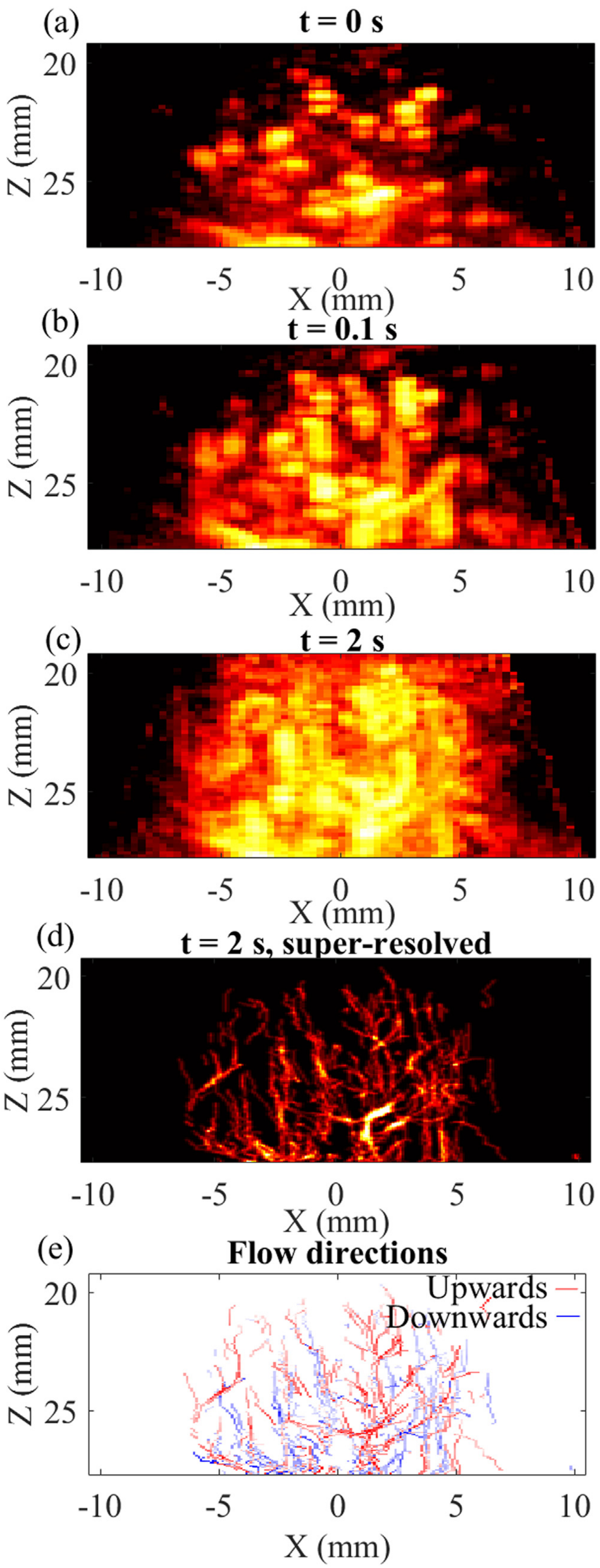

Figure 5. Maximum-intensity projections onto the xz plane of power Doppler volumes after accumulation in time. (a) At $t = 0$ s (or single frame), single microbubbles can still be distinguished. As the accumulation time increases, the sum of locations where the sparse bubble population have been maps out the vasculature (b, c). The low resolution of the power Doppler volumes makes it difficult to distinguish vascular structure. After super-resolution processing, individual vessels are visible (d). A 3-D rendered video of the super-resolution result can be found in the supplementary material (online only). (e) Microbubble movement direction in the kidney cortex: upward and downward moving bubbles were labeled ***red*** and ***blue***, respectively.

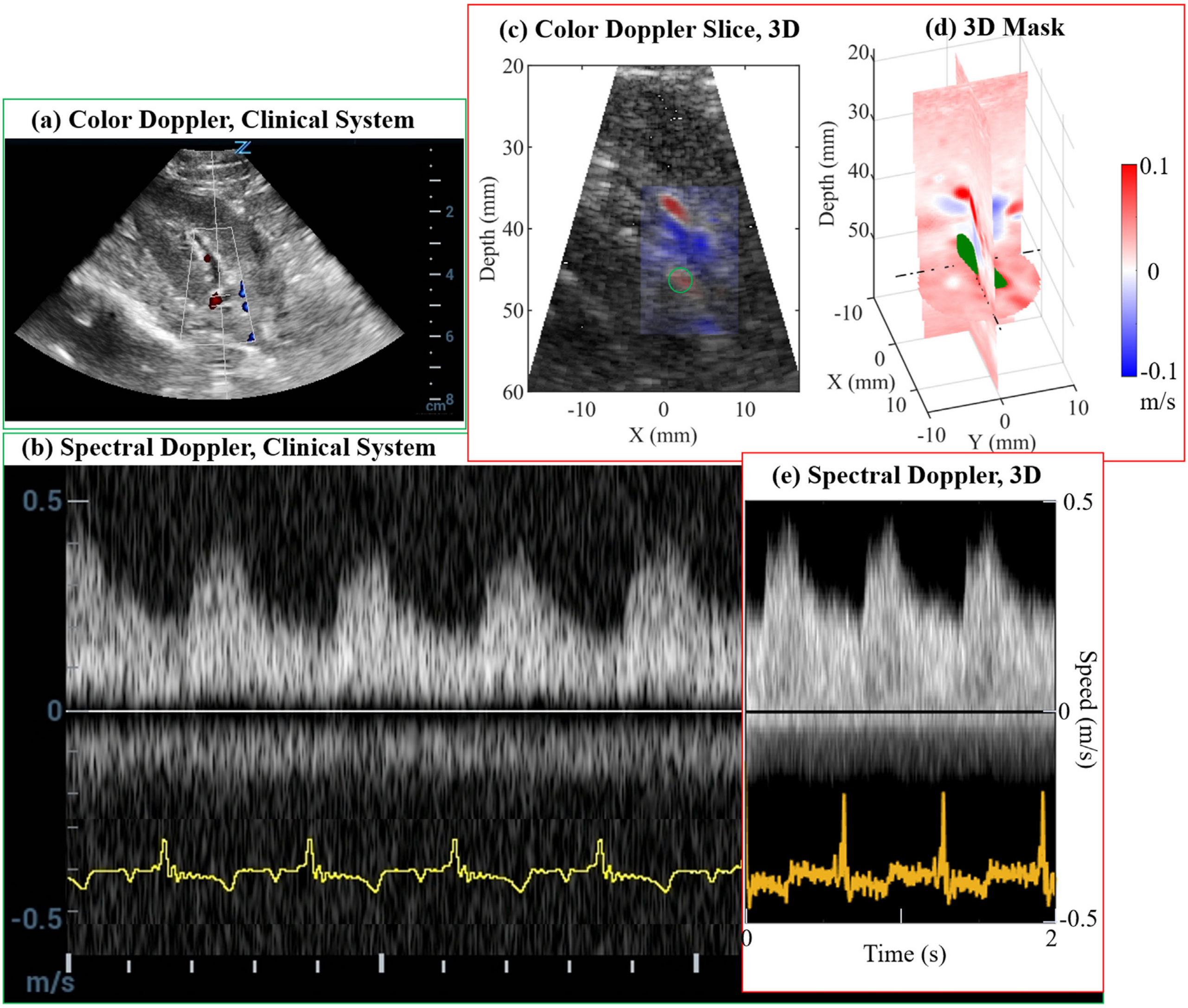

Figure 6. (a) Color Doppler overlayed on the B-mode image of the kidney taken using the clinical system with a P4-1C probe (Zonare, San Jose, CA, USA). The color Doppler image was used to select a vessel underneath the renal cortex for spectral Doppler measurements. The range gate was placed on this vessel. (b) Spectral Doppler results from the clinical system showed a pulsatile flow within this artery. The same kidney was measured using the 3-D probe and similar color and spectral Doppler results were obtained. (c) One of the color Doppler frames overlayed on top of a focused-beam B-mode image. The ***green circle*** labels the artery of interest. (d) Slices through the 3-D color Doppler volume and the 3-D manually selected segmentation mask in ***green***. The 3-D mask was used for spectral Doppler measurements of the segmented artery, in which the flow speed was calculated based on the angle between the vessel and the transmit beam in three dimensions.

low concentrations of microbubbles, in-probe amplifiers and SC beamforming, we could achieve high-quality, high-frame-rate, contrast-enhanced volumetric images.

The high transmission/reception system flexibility enabled us to achieve a variety of imaging modalities. On top, focused-beam imaging was performed in real time by cross-plane imaging to identify the imaging targets during the experiments. Increasing the frame rate with focused beams could also be done either by transmitting wider single beams or multiple beams at the same time [21,22]. The achievable high frame rates can potentially be used for elastography, albeit that the high clutter levels may represent a challenge.

There are a few drawbacks of the current system that require further improvement. The probe opening angle is narrow (30°) compared with the standard phased arrays currently used in the clinical setting (>90°). This limited our ability to visualize the entire kidney at once. Designing probes with smaller elements would increase the opening angle, but at the detriment of transmit and receive sensitivity. Further hardware developments are needed in this area. The current implementation of the SC beamformer has high resource requirements and long processing time, thus preventing real-time volumetric feedback while scanning. Improved implementation, other coherence-based beamformers or machine learning approaches for image reconstruction should be investigated in the future to provide real-time feedback of the scanned region and the data quality. Lastly, poor B-mode quality of the volumetric image does not allow lesion identification without contrast injection. Because of cross-talk between elements, contrast-to-background levels of this prototype probe are low [24]. B-mode images likely do not have high enough contrast for small-lesion identification, while contrast injection for this purpose may pose a hurdle to clinical adaptation of this technique. Hardware improvements (such as reducing element cross-talk, increasing element sensitivity uniformity) for future protypes are needed to improve B-mode image quality.

With our imaging system, the kidney structure as well as blood flow on both local and global scales can be investigated at the same time. Doppler in the large vessels enables traditional global perfusion estimators such as the resistive index to be calculated. Thanks to volumetric recordings, inaccuracies caused by out-of-plane flow should be eliminated, making estimations more accurate and robust. With super-resolution imaging of the kidney cortex, local perfusion or blood flow defects can potentially be identified. This kind of information can aid future research on kidney diseases.

Conclusions

We have determined high-frame-rate volumetric transcutaneous porcine renal vasculature imaging using a home-built sparse spiral array and ultrasound contrast agents. We could visualize capillary as well as interlobular vessels in three dimensions using a spatial coherence beamformer. We could further delineate microvasculature in the cortex and measure flow directions by performing super-resolution imaging techniques from the freehand 2 s recording. We could measure blood flow in the interlobular vessels using Doppler ultrasound. These results indicate, in a large-animal model, the extensive imaging flexibility of sparse spiral array *in vivo*.

Conflict of interest

The authors declare no competing interests.

Acknowledgments

The authors thank Henry den Bok (TU Delft) for the design and implementation of electronics, Boudewine Ossenkoppele (TU Delft) for her help on probe characterization, Mihai Strachinaru (EMC) for preliminary imaging experiments, Joaquim Bobi I Gibert (EMC) and Annemarie Verzijl (EMC) for their support during the animal experiments and Jason Voorneveld (EMC) for helpful discussions and code sharing.

This work was part of the research program Vernieuwingsimpuls—Vidi 2017 (Project No. QUANTO-16572), which is (partly) financed by the Dutch Research Council (NWO). This work was also partially supported by the Moore4Medical project funded by the ECSEL Joint Undertaking under Grant No. H2020-ECSEL-2019-IA-876190 and by the Italian Ministry of University and Research (PRIN 2020) under Grant No. 20205HFXE7.

Data availability statement

The data that support the findings of this study are available from the corresponding author on reasonable request.

Supplementary materials

Supplementary material associated with this article can be found in the online version at doi:10.1016/j.ultrasmedbio.2023.08.009.

References

[1] Spatola L, Andrulli S. Doppler ultrasound in kidney diseases: a key parameter in clinical long-term follow-up. J Ultrasound 2016;19:243–50.
[2] Gameraddin M. Ultrasound of the kidneys: application of Doppler and elastography. In: Gamie SAAG, Foda EM, editors. Essentials of abdominal ultrasound. IntechOpen; 2019.
[3] Petrucci I, Clementi A, Sessa C, Torrisi I, Meola M. Ultrasound and color Doppler applications in chronic kidney disease. J Nephrol 2018;31:863–79.
[4] Perrella RR, Duerinckx AJ, Tessier FN, Danovitch GM, Wilkinson A, Gonzalez S, et al. Evaluation of renal transplant dysfunction by duplex Doppler sonography: a prospective study and review of the literature. Am J Kidney Dis 1990;15:544–50.
[5] Mahoney M, Sorace A, Warram J, Samuel S, Hoyt K. Volumetric contrast-enhanced ultrasound imaging of renal perfusion. J Ultrasound Med 2014;33:1427–37.
[6] Arima M, Takahara S, Ihara H, Ichikawa Y, Ishibashi M, Sagawa S, et al. Predictability of renal allograft prognosis during rejection crisis by ultrasonic Doppler flow technique. Urology 1982;19:389–94.
[7] Izumi M, Sugiura T, Nakamura H, Nagatoya K, Imai E, Hori M. Differential diagnosis of prerenal azotemia from acute tubular necrosis and prediction of recovery by Doppler ultrasound. Am J Kidney Dis 2000;35:713–9.
[8] Fischer K, Can Meral F, Zhang Y, Vangel MG, Jolesz FA, Ichimura T, et al. High-resolution renal perfusion mapping using contrast-enhanced ultrasonography in ischemia−reperfusion injury monitors changes in renal microperfusion. Kidney Int 2016;89:1388–98.
[9] Zhang JL, Lee VS. Renal perfusion imaging by MRI. J Magn Reson Imaging 2020;52:369–79.
[10] Grenier N, Cornelis F, le Bras Y, Rigou G, Boutault JR, Bouzgarrou M. Perfusion imaging in renal diseases. Diagn Interv Imaging 2013;94:1313–22.
[11] Mercado MG, Smith DK, Guard EL. Acute kidney injury: diagnosis and management. Am Fam Physician 2019;100:687–94.
[12] Christensen-Jeffries K, Browning RJ, Tang MX, Dunsby C, Eckersley RJ. In vivo acoustic super-resolution and super-resolved velocity mapping using microbubbles. IEEE Trans Med Imaging 2015;34:433–40.
[13] Christensen-Jeffries K, Couture O, Dayton PA, Eldar YC, Hynynen K, Kiessling F, et al. Super-resolution ultrasound imaging. Ultrasound Med Biol 2020;46:865–91.
[14] Yi HM, Lowerison MR, Song PF, Zhang W. A review of clinical applications for super-resolution ultrasound localization microscopy. Curr Med Sci 2022;42:1–16.
[15] Chen Q, Yu J, Rush BM, Stocker SD, Tan RJ, Kim K. Ultrasound super-resolution imaging provides a noninvasive assessment of renal microvasculature changes during mouse acute kidney injury. Kidney Int 2020;98:355–65.
[16] Huang SF, Chang RF, Moon WK, Lee YH, Chen DR, Suri JS. Analysis of tumor vascularity using three-dimensional power Doppler ultrasound images. IEEE Trans Med Imaging 2008;27:320–30.
[17] Hoyt K, Sorace A, Saini R. Quantitative mapping of tumor vascularity using volumetric contrast-enhanced ultrasound. Invest Radiol 2012;47:167–74.
[18] Huang Q, Zeng Z. A review on real-time 3D ultrasound imaging technology. Biomed Res Int 2017;2017:6027029.
[19] Harput S, Christensen-Jeffries K, Ramalli A, Brown J, Zhu J, Zhang G, et al. 3-D super-resolution ultrasound imaging with a 2-D sparse array. IEEE Trans Ultrason Ferroelectr Freq Control 2020;67:269–77.
[20] Wang D, Zhang J, Zhang J. Matrix array 3D contrast-enhanced imaging of rabbit kidney in vivo using random sparse apertures. Proc IEEE Int Ultrason Symp 2021;2021:1–2.
[21] Roux E, Varray F, Petrusca L, Cachard C, Tortoli P, Liebgott H. Experimental 3-D ultrasound imaging with 2-D sparse arrays using focused and diverging waves. Sci Rep 2018;8:1–12.
[22] Ramalli A, Harput S, Bezy S, Boni E, Eckersley RJ, Tortoli P, et al. High-frame-rate tri-plane echocardiography with spiral arrays: from simulation to real-time implementation. IEEE Trans Ultrason Ferroelectr Freq Control 2020;67:57–69.
[23] Ramalli A, Boni E, Giangrossi C, Mattesini P, Dallai A, Liebgott H, et al. Real-time 3-D spectral Doppler analysis with a sparse spiral array. IEEE Trans Ultrason Ferroelectr Freq Control 2021;68:1742–51.
[24] Wei L, Boni E, Ramalli A, Fool F, Noothout E, van der Steen AFW, et al. Sparse 2-dimensional PZT-on-PCB arrays with density tapering. IEEE Trans Ultrason Ferroelectr Freq Control 2022;69:2798–809.
[25] Wei L, Wahyulaksana G, Meijlink B, Ramalli A, Noothout E, Verweij MD, et al. High frame rate volumetric imaging of microbubbles using a sparse array and spatial coherence beamforming. IEEE Trans Ultrason Ferroelectr Freq Control 2021;68:3069–81.
[26] Boni E, Fool F, Verweij MD, Vos HJ, Tortoli P. On the efficacy of in-probe pre-amplifiers for piezoelectric 2D arrays. Proc IEEE Int Ultrason Symp 2020;2020:1–4.
[27] Rodriguez-Molares A, Rindal OMH, Bernard O, Nair A, Bell MAL, Liebgott H, et al. The ultrasound toolbox. Proc IEEE Ultrason Symp 2017;2017:1–4.
[28] Pnevmatikakis EA, Giovannucci A. NoRMCorre: an online algorithm for piecewise rigid motion correction of calcium imaging data. J Neurosci Methods 2017;291:83–94.
[29] Couture O, Hingot V. Short course: super-resolution ultrasound. Proc IEEE Ultrason Symp 2020;2020:1–4.
[30] Chade AR. Renal vascular structure and rarefaction. Compr Physiol 2013;3:817.
[31] Nabeshima Y, Seo Y, Takeuchi M. A review of current trends in three-dimensional analysis of left ventricular myocardial strain. Cardiovasc Ultrasound 2020;18:1–21.
[32] Macé E, Montaldo G, Cohen I, Baulac M, Fink M, Tanter M. Functional ultrasound imaging of the brain. Nat Methods 2011;8:662–4.
[33] Voorneveld J, Saaid H, Schinkel C, Radeljic N, Lippe B, Gijsen FJH, et al. 4-D echo-particle image velocimetry in a left ventricular phantom. Ultrasound Med Biol 2020;46:805–17.
[34] Hansen-Shearer J, Lerendegui M, Toulemonde M, Tang MX. Ultrafast 3-D ultrasound imaging using row−column array-specific frame-multiply-and-sum beamforming. IEEE Trans Ultrason Ferroelectr Freq Control 2022;69:480–8.